The Effect of Hydrostatic Stress on Magnetic Properties of Mn-Zn Power Ferrites at Varying Excitation Levels

Ibrahim Ellithy [1,†,‡,*] , Mauricio Esguerra [1,‡] and Rewanth Radhakrishnan [1]

[1]   Magment GmbH, 82041 Oberhaching, Germany.
[*]   Correspondence: Ibrahim.ellithy@magment.co;
[†]   Current address: Raiffeisenallee 12b, 82041 Oberhaching, Germany.
[‡]   These authors contributed equally to this work.

Abstract: In this paper, the effects of hydrostatic stress on the magnetic properties of MnZn power ferrites are discussed. Ring cores were embedded in cement and the curing process gradually exerted pressure on the core. A novel testing method was developed to continuously measure the power losses and the magnetic susceptibility in dependence on magnetic excitation at a fixed frequency and room temperature with a Vector Network Analyzer. After 450 hours, a maximum compressive stress of 120 MPa was reached. Power loss up to 300% was observed, while magnetic susceptibility dropped by 35%. The magneto-mechanical effect on core losses was simulated with the Hodgdon-Esguerra hysteresis model, showing excellent agreement with tested results, which allows to predict the behavior of ferrite tiles embedded in load-bearing surfaces for Wireless Power Transfer (WPT) applications.

Keywords: Hydrostatic Stress; Mn-Zn ferrites; Cement; Magnetic; Core Losses; WPT

1. Introduction

Power magnetic materials are characterized by low losses at high excitations, which means they can be designed for compact devices that play a crucial role in many electrical and electronic applications like inductive wireless power transfer (WPT) systems [1]. Soft magnetic materials for inroad charging systems are encapsulated or even embedded under a road or floor [2–6], therefore the exploration of the behavior under applied pressure holds considerable concerns to evaluate the efficiency of the WPT systems. Previous research has been oriented to conventional inductive components with a focus on the effect of stress on susceptibility [7–9]. A li et al. studied the stress effect on power loss of Mn-Zn ferrites for high-frequency applications [10]. However, there are no studies on the stress effect on power losses at frequencies below 100 kHz and mid-excitation levels as used for example for WPT. This has direct implications for advancing our current technological infrastructure, where there's a need to embed transmitter coils beneath roads or floor surfaces.

To truly test the capabilities of these materials and understand their behavior under pressure, it becomes imperative to deploy innovative and easily implementing testing methodologies. In this light, our research introduces a novel approach where we subject MnZn ferrite samples to hydrostatic pressure, simulating this by embedding them in cement during its curing phase. This method offers a real-world approximation of the stresses and pressures these materials might experience when integrated into transportation infrastructure.

For our experimental evaluations, we employed the Vector Network Analyzer Bode 100. This choice was motivated by the device's versatility, especially adept at handling tests up to mid-excitation levels, even with relatively smaller core samples. However, pure empirical data, though invaluable, often benefits from theoretical underpinnings. Thus, to contextualize our observations, we drew upon established hysteresis models [11,12]. These models offer a robust framework to interpret our experimental findings. Moreover, they serve as an essential tool in predicting the behavior of these materials within specific environmental parameters, ensuring that our results are both grounded in theory and pertinent to real-world applications.

2. Materials and Methods

2.1. Samples Preparation

The study prominently featured MnZn ferrite cores manufactured by TDK and DMEGC. The N87 ferrite, characterized by its R12.5/7.5/5 toroid configuration epoxy coated, and the DMR95 epoxy coated variant, characterized by its R22/14/8 toroid configuration, were deliberately selected for the purpose of investigating the subtle alterations in magnetic properties induced by hydrostatic stress.

The selected embedding medium was Universal Cement, a cementitious binder manufactured by Sakret (DIN EN 197). The selection of this binder was done to replicate embedding situations observed in real-world settings, aiming to generate hydrostatic pressure during the curing process. The initial stage of sample preparation began with the diligent inspection of the MnZn ferrites cores. Both the N87 and DMR95 were inspected for defects or irregularities. part of the preparation of these ferrites involved winding them to enable magnetic property measurements.

Figure 1. N87 and N95 Ferrite Cores Tested.

Figure 1 shows the DMR95 toroid carefully wounded with $N = 10$ turns, while the two N87 cores stacked and wounded with $N = 12$ turns. This winding configuration and the number of cores n used were chosen to enable precise monitoring of the magnetic parameters at the highest excitation levels possible according to equation (1).

$$\hat{J} = \frac{2V_{\text{rms}}\sqrt{2}}{NnA_e 2\pi f} \cdot \frac{\omega L}{\sqrt{(\omega L)^2 + R_i^2}} \tag{1}$$

A_e is the effective area of one core, R_i is the internal resistance of the device. Both samples were hand-wound using Tuofeng 28AWG 0.080 mm² with PVC insulation to prevent water penetration. The volume-defined plastic container was used to embed the two cores and monitor the volume of the poured cement.

Cement paste without aggregates is characterized by inherently higher internal stresses due to the absence of aggregates which serve as an internal restraint in concrete. These are pronounced further by higher water-to-cement (w/c) ratios [13,14]. For the embedding process, a precise mixture of Universal Cement from Sakret was prepared without any aggregates and with a 0.65 water-cement ratio. Each ferrite ring, post-winding, was gently encased within the cement, ensuring uniform encapsulation.

2.2. experimental setup

A parallel sensing system was developed to capture a variety of environmental variables throughout the curing process. The DS18B20 Digital Stainless Steel Temperature Sensor with accuracy $\pm 0.5°$C measured the temperature. The incorporation of the Gardena Soil Moisture Sensor, developed by iHaospace, serves the purpose of measuring moisture levels, which is a critical variable in understanding the processes involved in curing. Figure 2 shows the schematic diagram of the test setup.
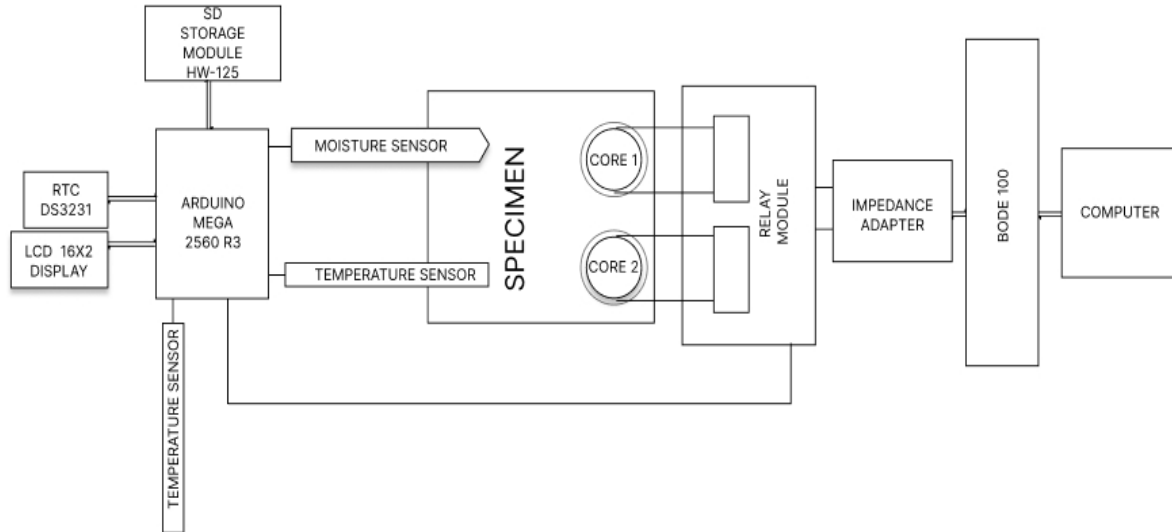

Figure 2. Test setup schematic diagram.

In addition to the aforementioned sensor suite, an advanced control circuit was devised. The primary function of the Arduino Mega microcontroller was to collect and analyze data obtained from the integrated sensors. In order to maintain temporal precision, the integration of a Real-Time Clock (RTC) was synchronized with the data stream, assigning timestamps to every recorded measurement. The data was collected at precise intervals of one minute and stored sequentially using an external storage solution that utilized a Micro SD TF Card Adapter Reader Module. This allowed for a detailed record of the whole process of curing. Table 1 shows the hardware components used in the experiment with detailed functions of each.

Table 1. List of the hardware components used in the experiment .

Component	Model Number	Function
Motherboard	Arduino Mega 2560 R3	Data Collection and analysis
Real time clock	DS3231	Time Recording of the measurements
SD storage Module	HW-125	data saving
Moisture sensor	SOIL478	measuring the moisture content inside the cement
Temperature sensor	DS18B20	Temperature measurement
LCD display	HD44780	Display Real-time Data
Relay	-	Controlling the DUT with Bode100

2.3. Testing Method and Automation

The evaluation of the magnetic properties is done using Vector Network analyzer Bode 100. Bode 100 is a versatile device that is able to perform impedance analysis on the specimen, and the frequency response of the sample inductance and resistance will be measured. A new method is being used to vary the frequency with the source output level

V_{rms} of Bode 100. Figure 3 shows the linear relation between the frequency and the output voltage signal.
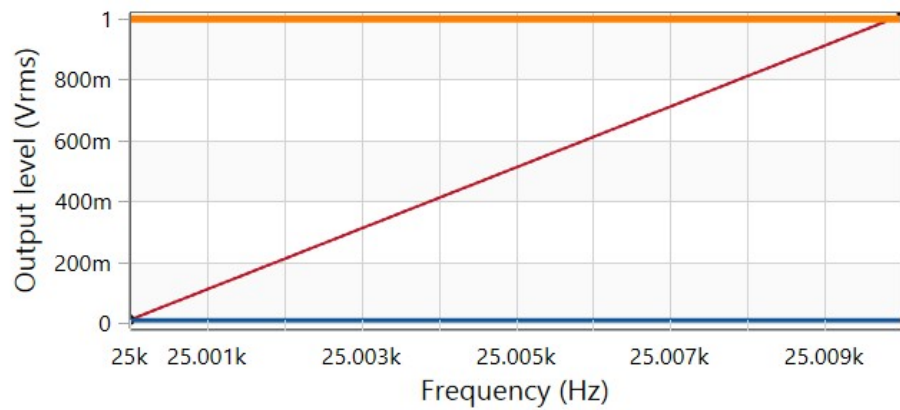

Figure 3. The Relation between the Frequency and output Voltage of Bode100 Software.

The frequency range was chosen to be statistically insignificant with a range of 0.01 kHz which will allow a varying voltage output at an approximately constant frequency of 25 kHz. The excitation levels will vary in relation to the voltage according to equation (1).

This analysis has been automated to measure the reading at a fixed interval, over an extended period of time, to study the gradual change in the material properties with respect to change in its environment which is also being monitored and recorded using an external microcontroller setup.

There are a few methods to automate the Bode 100. Python was chosen for its versatility and data post-processing ability. Bode 100 is operated using a Python environment. Bode 100 provides a library that can be used to automatically execute the measurements [15]. The parameters used for the measurement of the properties are presented in Table 2.

Table 2. Bode100 Parameters for automatic testing.

Property	Setting
Measurement Type	Impedance measurement through adapter
Measurement frequency range	25000Hz – 25010Hz
Sweep Mode	Logarithmic
Measurement points	201
Source Shaping Level - 1	Output Level 0.01V @ 25000Hz
Source shaping Level - 2	Output level 0.998815 @ 25010Hz

An external calibration file containing the calibration data of the full frequency range and user frequency range, are required in order to perform the impedance test. The calibration can be performed using the bode suite, and the calibration file can be exported with the file extension "mcalx", which will be later loaded in the python environment to execute the measurement. Once the measurement is executed. The results are available in array format, which be exported as a csv file, with the frequency, to plot the graph and to observe the trend over the frequency range. The measurement of multiple samples using the same adapter is performed using a relay board which is controlled by Arduino microcontroller. They are in sync to switch between the coil connections and the measurement being executed and saved with a unique file name denoting the core that is being measured.

2.4. Data Evaluation

The data directly exported from the Bode100 vector network analyzer were leveraged, ensuring a systematic and precise data acquisition process. Fundamental to the analysis were the L_s and R_s values; these parameters were essential for deriving both the power loss

and magnetic susceptibility of the samples. Over a rigorous evaluation period of time till the susceptibility change saturated, The behavior of MnZn ferrite samples was observed and recorded. An automated Python code was generated to evaluate the magnetic susceptibility and core losses at a time step of 30 mins according to the settings of the automated Bode100 program. The magnetic susceptibility was calculated according to equation (2).

$$\chi = \frac{L_s}{\mu_0 N^2} \cdot \frac{le}{Ae} - 1 \tag{2}$$

l_e is the effective length. The values of R_s were used to calculate $\tan(\delta)$ according to equation (3) and hence to calculate the core power losses according to equation (4).

$$\tan \delta = \frac{R_s - R_{\mathrm{DC}}}{\omega L} \tag{3}$$

$$P_v = \frac{\pi \tan \delta \hat{J}^2 f}{\mu_0 \chi} \tag{4}$$

3. Results

3.1. Magnetic Susceptibility

The analysis of magnetic susceptibility spanned a magnetic polarization range from 0.25 to 50 mT. Ferromagnetic materials exhibit more linear behavior at low excitations and this allows better characterization of the material's intrinsic magnetic properties without saturation effects as shown in Figure 4 and Figure 5. The value of the magnetic susceptibility at 1 mT was considered for the comparison. Initial observations highlighted a surge in susceptibility because of the increase in temperature [16], a phenomenon related to the exothermic reactions inherent in the cement curing process. As the experiment progressed, this initial increment in susceptibility was succeeded by a discernible decline. Figure 4 and Figure 5 show the drop of the susceptibility correlated strongly with the escalating hydrostatic pressure exerted on the MnZn power ferrites N87 and DMR95. The monitoring spanned a 17-day period until the applied pressure stopped increasing and susceptibility stabilized.
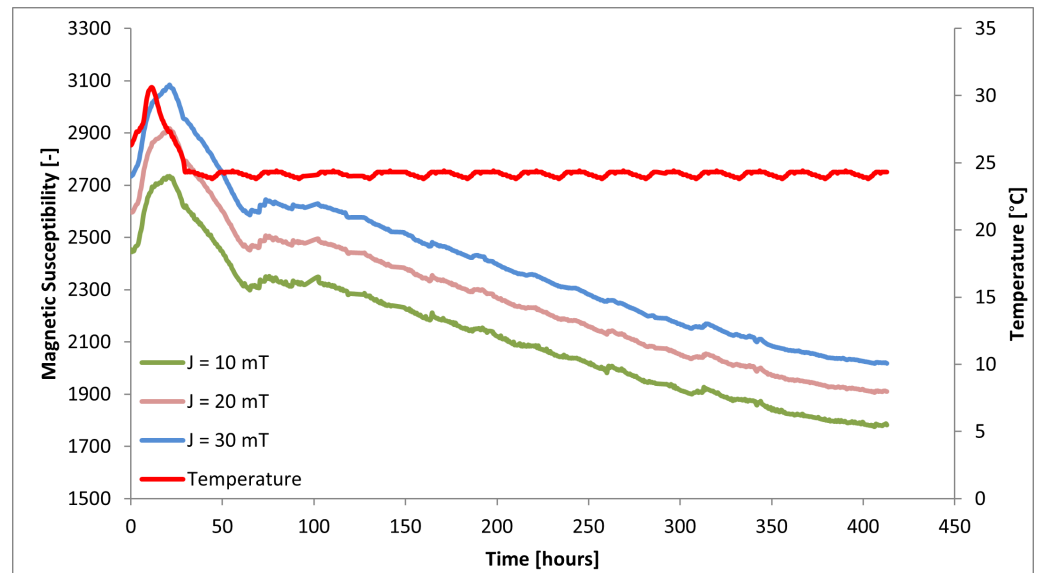

Figure 4. Magnetic Susceptibility change over time of N87 core.

The percentage reduction of susceptibility depends closely on the ferrite material [17]. During the Experiment, the susceptibility saturated and encountered a drop of 32.08% and 53.57% at 25°C for N87 and DMR95 ferrite grades respectively.
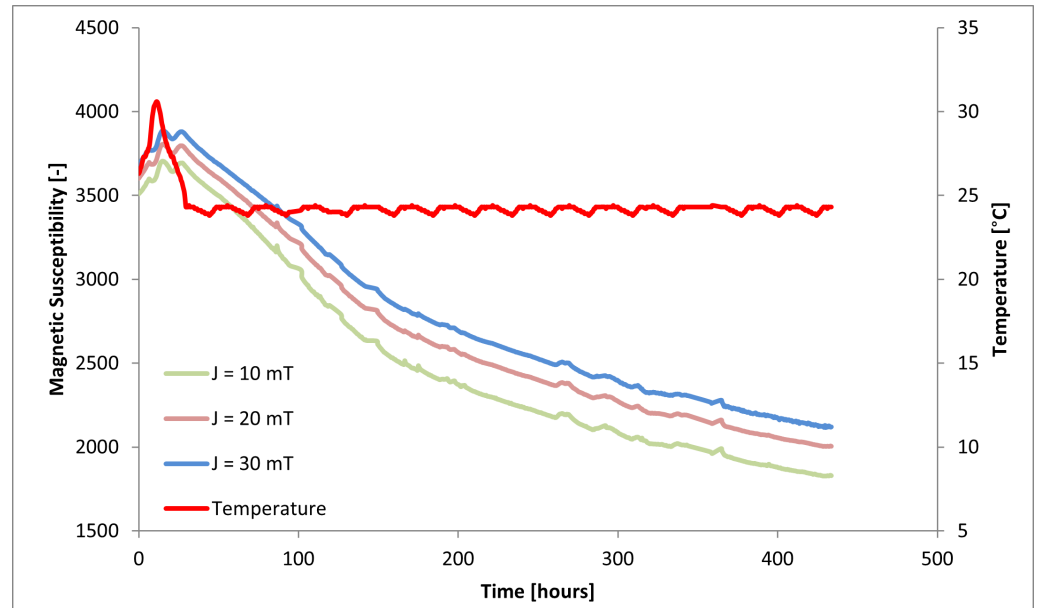
Figure 5. Magnetic Susceptibility change over time of DMR95 core.

3.2. Core Losses

The method used to measure the power loss allowed precise monitoring at different excitation levels, The losses at 10 mT, 20 mT, and 30 mT were evaluated and compared over 17 days of curing. The percentage increases with respect to the original value of the toroids before embedding in the cement mixture. Table 3 shows the percentages at different excitation levels and under the conditions of ΔP_v (%) at $\Delta \chi$ of -10%, ΔP_v (%) at $\Delta \chi$ of -20%, and ΔP_v (%) at $\Delta \chi$ of -30% for N87 and DMR95. The losses increase are more profound at low excitation levels and the percentage decreases with the increase of the polarization. Measurements on a power ferrite at 100 mT show a loss increase of $+1.3\% \, \mathrm{MPa}^{-1}$ [18].

Table 3. The percentage change of power loss of DMR95 and N87 at different percentages drop of susceptibility and excitation levels.

J	Ferrite Grade	ΔP_v at $\Delta \chi$ of -10%	ΔP_v at $\Delta \chi$ of -20%	ΔP_v at $\Delta \chi$ of -30%
	N87	17.2%	35.2%	66.3%
10 mT	DMR95	73.5%	158.5%	243.1%
	N87	14.4%	32.8%	59.3%
20 mT	DMR95	59.7%	131.7%	201.1%
	N87	10.5%	28.7%	50.8%
30 mT	DMR95	51.6%	115%	172.8%

The loss measurements under the hydrostatic pressure were carried out at room temperature (25°C), Figure 6 and Figure 7 show the change in power loss as a function of the time under different excitation levels of 10 mT, 20 mT, and 30 mT of N87 and DMR95.
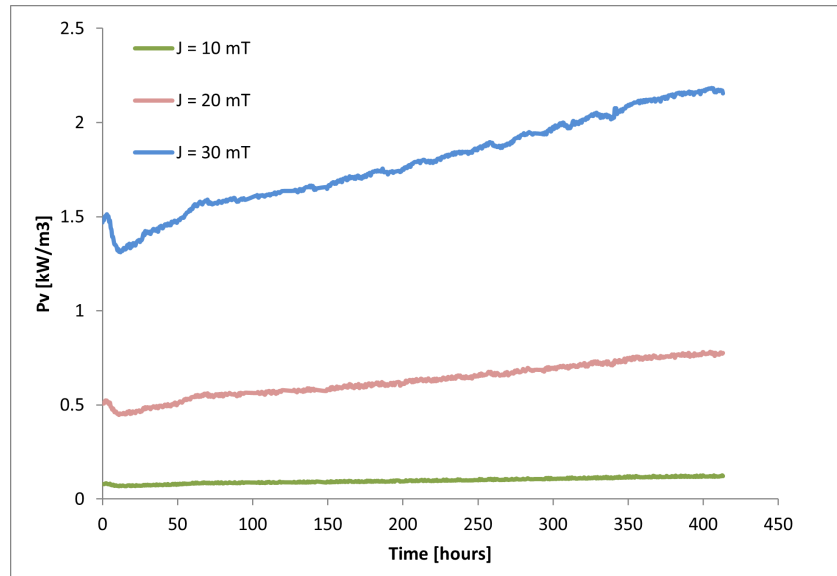
Figure 6. Power loss for the N87 Mn–Zn ferrite core under the conditions of 25 kHz/10 mT, 25 kHz/20 mT and 25 kHz/30 mT.

At all excitation levels of 10, 20, and 30 mT, P_v increased with the ongoing curing process of cement and hence the increasing internal stresses. When reaching the point at which the susceptibility changes saturated, the hydrostatic pressure was calculated corresponding to a value of σ = 120 MPa using Equation (5) by assuming $k = 3 \times 10^{-6} \frac{1}{\text{MPa}}$ [19] .

$$\frac{1}{\chi(\sigma)} = \frac{1}{\chi_i} + k \cdot \sigma \tag{5}$$

For N87 the losses P_v at 10 mT increased from 0.07 to 0.12 kW/m^3, P_v at 20 mT increased from 0.47 to 0.77 kW/m^3, and P_v at 30 mT increased from 1.40 to 2.15 kW/m^3. For DMR95 the losses P_v at 10 mT increased from 0.02 to 0.14 kW/m^3, P_v at 20 mT increased from 0.12 to 0.67 kW/m^3, and P_v at 30 mT increased from 0.33 to 1.50 kW/m^3.
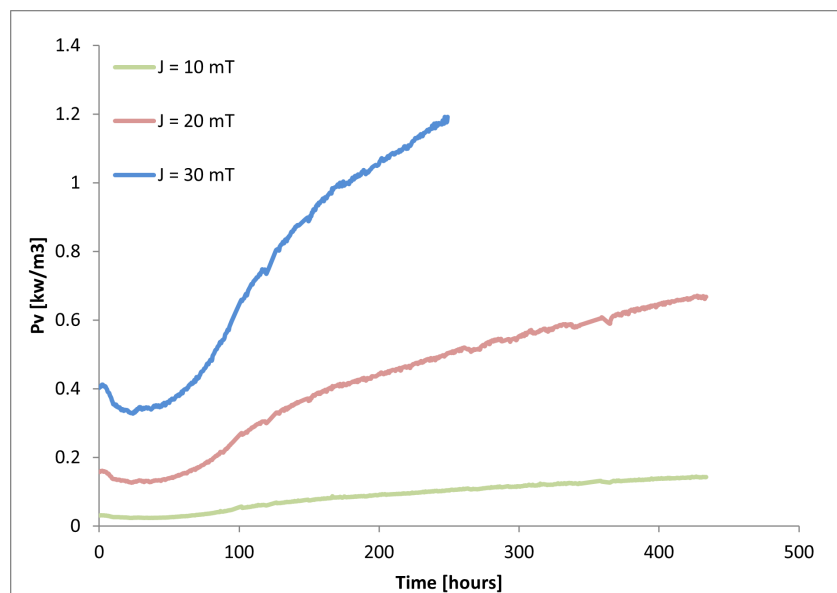

Figure 7. Hydrostatic pressure dependence of power loss for the N87 Mn–Zn ferrite core under the conditions of 25 kHz/15 mT, 25 kHz/25 mT and 25 kHz/30 mT.

4. Discussion

4.1. hysteresis Model

The increase of losses with hydrostatic pressure was modeled with the Hodgdon-Esguerra differential equation hysteresis model [11,12]. For magnetic polarisations $J < \frac{J_s}{2}$, specific power loss can be expressed by Equation (6).

$$P_v = \frac{8}{3} \cdot f^{1+x} \cdot Hc \cdot \left[1 - \sqrt{(1 - \frac{J}{Js})^{\alpha_0(\sigma) \cdot Js} \cdot [2 - (1 - \frac{J}{Js})^{\alpha_0(\sigma) \cdot Js}]} \right] \tag{6}$$

H_c is the coercive field, x depends on the material and varies between 0 and 1, and J_s is the saturation. The dependence of the exponent on mechanical stress σ is related to the change of susceptibility χ with pressure according to Equation (7).

$$\alpha_0(\sigma) = \frac{1}{\mu_0 H_c \chi_i} \cdot (1 - c \cdot \frac{\chi_i(\sigma)}{\chi_i(0)}) \tag{7}$$

Hc is the coercive field and c is the reversibility coefficient, defined as the ratio of the initial to the coercive susceptibility as shown in Equation (8).

$$c = \frac{\chi_i}{\chi_c} \tag{8}$$

However, since with the cement curing testing method, there is no pressure applied, there is no need to consider the explicit variation of power loss with compressive stress. Measurements are therefore compared to the hysteresis loss model by showing the percent loss increase ΔPv in dependence of the susceptibility drop $\Delta \chi$ as seen in Figure 8 and Figure 9 for DMR95 and N87 respectively. There is an excellent agreement for both material grades with the hysteresis model parameters in Table 4.

Table 4. The hystresis model parameters

Parameter	N87	DMR95
H_c $[\frac{A}{m}]$	11	4.9
c [-]	0.5	0.75
χ_i [-]	2465	3371
J_s $[mT]$	490	530

The loss increase is more pronounced for lower excitations and for higher reversibility coefficients c, which is higher for high-quality material grades such as DMR95.
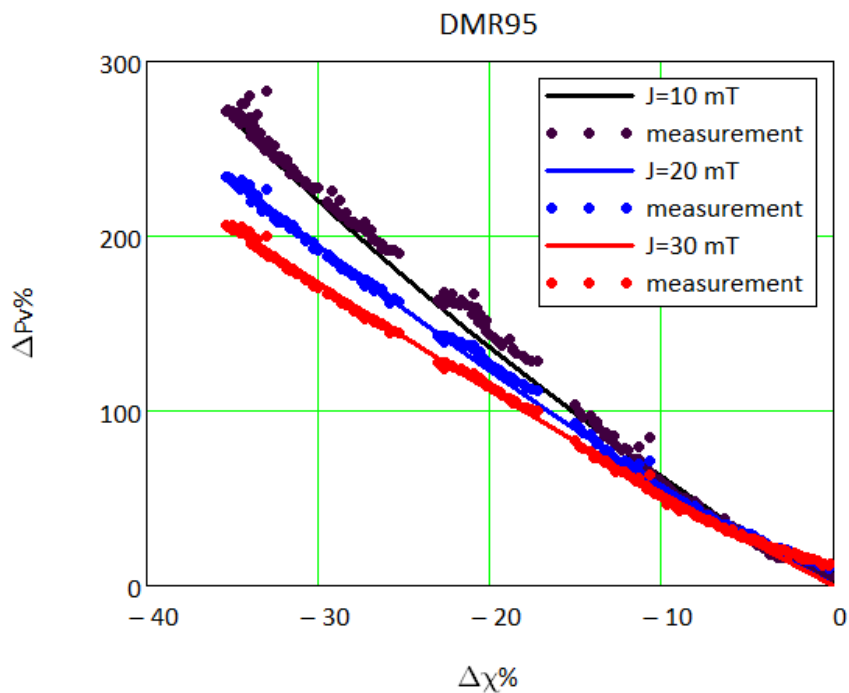
Figure 8. The percentage drop of susceptibility vs. the percentage drop of power losses at 10 mT, 20 mT, and 30 mT of DMR95.
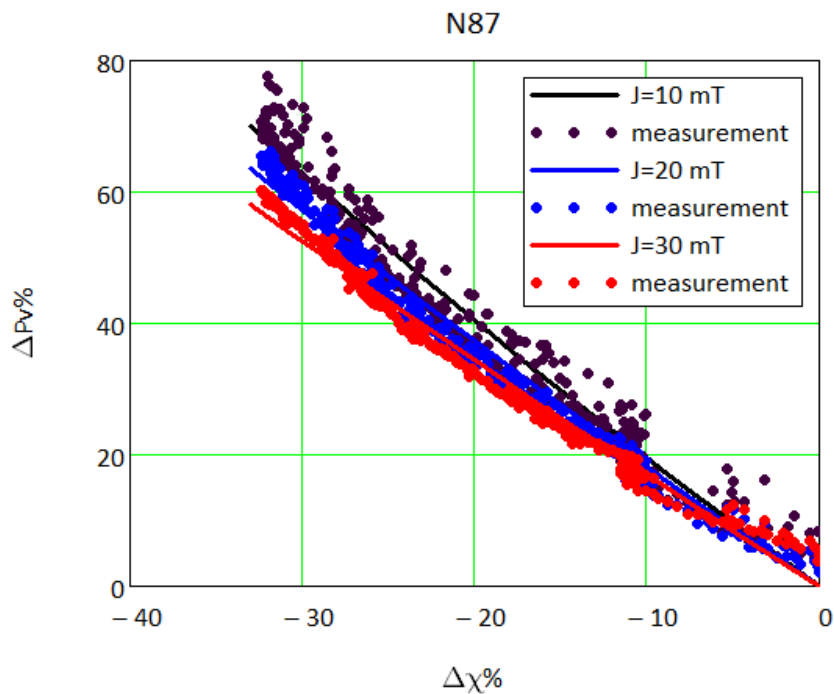

Figure 9. The percentage drop of susceptibility vs. the percentage drop of power losses at 10 mT, 20 mT, and 30 mT of N87.
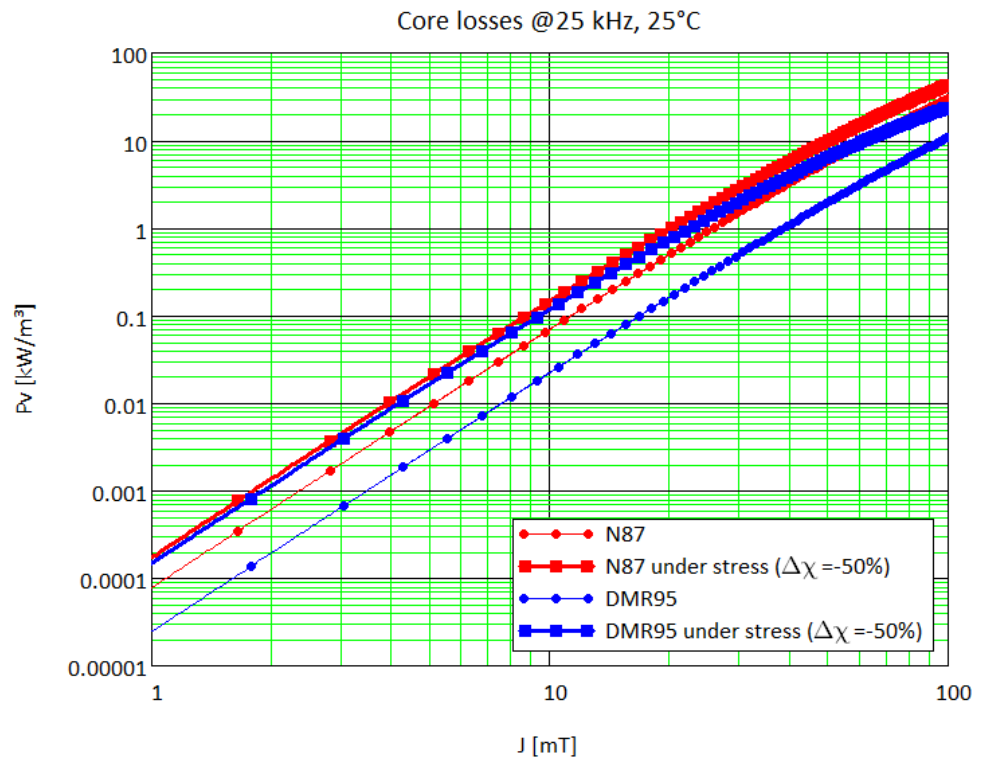
Figure 10. The calculated power loss vs. excitation in the double logarithmic graph.

The power loss vs. excitation can be then calculated with and without compressive stress yielding a susceptibility drop of -50%, which corresponds roughly to σ = 120 MPa. The power loss under stress is almost the same for DMR95 and N87 as shown in Figure 10.

5. Conclusions

Studying the magnetic properties of a soft magnetic material under hydrostatic pressure has led to several important conclusions. One key finding is that core loss increases significantly when the magnetic material is subjected to high pressure as a magneto-mechanical effect.

Another conclusion that can be drawn is based on the observation of core losses experienced by two different magnetic materials grades, namely DMR95 and N87, under the same conditions. DMR95 has much lower core losses compared to N87 under normal atmospheric room pressure. However, by increasing the applied pressure losses in both material grades increase. By saturation, the difference between the losses of the two grades became much smaller. This interpretation suggests that the extent of degradation in the magnetic property of a material under pressure depends on the inherent quality of that magnetic property itself.

This observed phenomenon has significant implications, especially in applications like WPT, where the transmitter coil is embedded into a road or floor. The difference in performance can be quite substantial when comparing the coil's efficiency before and after the embedment. In order to achieve optimal efficiency and performance in WPT, additional precautions and design considerations must be taken into account when enclosing the transmitter coil that is being embedded into a load-bearing surface such as a road or a floor. The understanding of this effect will help mitigate the adverse effects of pressure on the system.

Abbreviations

The following abbreviations are used in this manuscript:

WPT	Wireless Power Transfer
VNA	Vector Network Analyzer
RTC	Real Time Clock

References

1. Bosshard, R.; Kolar, J.W. Inductive power transfer for electric vehicle charging: Technical challenges and tradeoffs. *IEEE Power Electronics Magazine* **2016**, *3*, 22–30.
2. Eck, C. Betonfertigteile mit induktiver PRIMOVE Ladetechnik für Busline in Mannheim. *Heidelberg Cement, context magazine* **2015**, *2*, 36–37.
3. Ahn, S.; Pak, J.; Song, T.; Lee, H.; Byun, J.G.; Kang, D.; Choi, C.S.; Kim, E.; Ryu, J.; Kim, M.; et al. Low frequency electromagnetic field reduction techniques for the on-line electric vehicle (OLEV). In Proceedings of the 2010 IEEE International Symposium on Electromagnetic Compatibility. IEEE, 2010, pp. 625–630.
4. Gu, B.S.; Dharmakeerthi, T.; Kim, S.; O'Sullivan, M.J.; Covic, G.A. Optimised Magnetic Core Layer in Inductive Power Transfer Pad for Electric Vehicle Charging. *IEEE Transactions on Power Electronics* **2023**.
5. Aghcheghloo, P.D.; Larkin, T.; Wilson, D.; Holleran, G.; Amirpour, M.; Kim, S.; Bickerton, S.; Covic, G. The effect of an emulator inductive power transfer pad on the temperature of an asphalt pavement. *Construction and Building Materials* **2023**, *392*, 131783.
6. Trompetter, W.; Goddard-Winchester, M.; Li, K.Y.; Rumsey, B.; Leveneur, J.; Turner, J.; Chong, S.; Long, N.; Kennedy, J. Composite magnetic materials development for application in inroad charging systems. *Materials Today: Proceedings* **2023**.
7. Alley Jr, R.; Legg, V. Effects of hydrostatic pressure on the properties of magnetic materials. *Journal of Applied Physics* **1960**, *31*, S239–S240.
8. Bieńkowski, A.; Rożniatowski, K.; Szewczyk, R. Effects of stress and its dependence on microstructure in Mn–Zn ferrite for power applications. *Journal of magnetism and magnetic materials* **2003**, *254*, 547–549.
9. Baumann, M.; Sotier, S.; Weidinger, J. A model of initial permeability of soft ferrite in dependence of biaxial stress. *Journal of the Japan Society of Powder and Powder Metallurgy* **2014**, *61*, S70–S74.
10. Li, Z.; Ying, Y.; Wang, N.; Zheng, J.; Yu, J.; Li, W.; Qiao, L.; Cai, W.; Li, J.; Huang, H.; et al. Effect of compressive stress on power loss of Mn–Zn ferrite for high-frequency applications. *Ceramics International* **2022**, *48*, 17723–17728.
11. Esguerra, M. Modeling Hysteresis Loops of Soft Ferrite Materials. *8th International Conference on Ferrites, Kyoto* **2000**, pp. 220–222.
12. Hodgdon, M.L. Mathematical theory and calculations of magnetic hysteresis curves. *IEEE Transactions on Magnetics* **1988**, *24*, 3120–3122.
13. Neville, A.M.; Brooks, J.J. *Concrete technology*; Vol. 438, Longman Scientific & Technical England, 1987.
14. Neville, A.M.; et al. *Properties of concrete*; Vol. 4, Longman London, 1995.
15. Bode Automation Interface 3.25.2241.1. https://documentation.omicron-lab.com/BodeAutomationInterface/3.25SR1/index.html. Accessed: 2023-08-15.
16. TDK. Mn-Zn Ferrite, Material Characteristics. https://product.tdk.com/system/files/dam/doc/product/ferrite/ferrite/ferrite-core/catalog/ferrite_mn-zn_material_characteristics_en.pdf, 2022. Catalogue, Accessed: 2023-09-12.
17. Schweiger, A. Permeability and pressure in ferrite cores. *Siemens Components-English Edition* **1997**, *32*, 16–18.
18. Tsakaloudi, V.; Holz, D.; Zaspalis, V. The effect of externally applied uniaxial compressive stress on the magnetic properties of power MnZn-ferrites. *Journal of Materials Science* **2013**, *48*, 3825–3833.
19. Meuche, H.; Nguyen, A.H.; Lange, D.; Esguerra, M. influence of a mechanical stress on ferrite materials for broadband applications. *9th International Conference on Ferrites, San Francisco* **2004**, pp. 333–337.